Received: 17 January 2020 | Revised: 11 March 2020 | Accepted: 13 March 2020

DOI: 10.1002/jrs.5878

RESEARCH ARTICLE

Journal of RAMAN SPECTROSCOPY WILEY

Serial section Raman tomography with 10 times higher depth resolution than confocal Raman microscopy

Thomas Böhm[1,2] | **Riko Moroni**[3] | **Simon Thiele**[1,2]

[1]Forschungszentrum Jülich GmbH, Helmholtz-Institute Erlangen-Nürnberg for Renewable Energy (IEK-11), Erlangen, Germany

[2]Department of Chemical and Biological Engineering, Friedrich-Alexander-Universität Erlangen-Nürnberg, Erlangen, Germany

[3]Laboratory for MEMS Applications, IMTEK Department of Microsystems Engineering, University of Freiburg, Freiburg, Germany

Correspondence
Simon Thiele, Forschungszentrum Jülich GmbH, Helmholtz-Institute Erlangen-Nürnberg for Renewable Energy (IEK-11), 91058 Erlangen, Germany.
Email: si.thiele@fz-juelich.de

Funding information
German Federal Ministry of Education and Research (BMBF), Grant/Award Number: 03SF0536F

Abstract

Confocal Raman microscopy enables 3D imaging of various samples solely based on chemical contrast. However, optical artifacts impair resolution and image quality in subsurface imaging. With serial section Raman tomography, we show that serial ultrathin and semithin sectioning by ultramicrotomy can successfully be combined with subsequent confocal Raman imaging. This new 3D Raman imaging technique reaches a depth resolution of up to 100 nm, which is about 10-fold better than in confocal Raman microscopy. Structurally complex and optically inhomogeneous samples can not only be imaged, but also be used to quantify structural parameters. Serial section Raman tomography is a promising method for materials science and possibly also for life sciences.

KEYWORDS

polymer, Raman imaging, serial sectioning, tomography, 3D reconstruction

1 | INTRODUCTION

Confocal Raman imaging is a powerful microscopic technique that links the high spatial resolution of confocal laser scanning microscopy to the chemical sensitivity of Raman spectroscopy (Figure 1a). This combination enables spatially confined vibrational spectroscopy and can be employed to create images solely based on local spectral differences. With significant improvements in imaging speed and automated data processing in the last years, confocal Raman imaging and its related developments nowadays find applications in various fields, including, for example, biology, medicine, and pharmaceuticals.[1,2]

Especially in materials science, Raman imaging harbors great potential due to its ability of nondestructive imaging without the necessity to contrast samples prior to the analysis. For instance, imaging of polymers is often conducted with electron microscopy, although its application is challenging because of the high sensitivity of polymers toward radiation-induced damage and due to the low electron contrast of light elements such as carbon, oxygen, and hydrogen.[3] Many polymers are strong Raman scatterers, and already small deviations in the

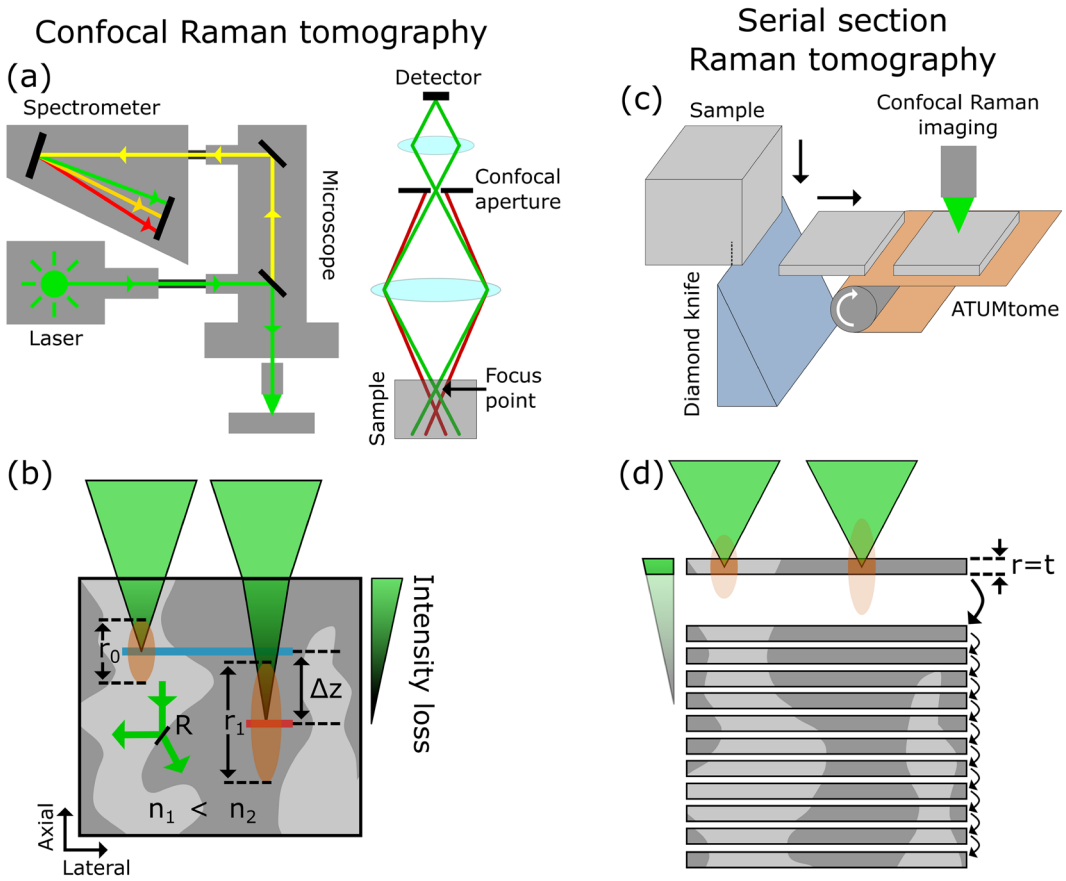

FIGURE 1 Comparison of confocal and serial section Raman tomography. (a) In confocal Raman microscopy, a microscope focuses a laser onto a sample, and Raman signals are collected by a spectrometer. The confocal aperture in the microscope's beam path blocks light from above and below the focus point to enable optical sectioning. (b) In case the refractive index (n) of a sample does not match the refractive index the objective is designed for (n_1, here with $n_2 > n_1$), spherical aberration occurs below the sample surface. Among the effects caused by refraction are a loss in intensity with increasing focus depth, a shift between apparent and actual focus depth (Δz, blue bar compared with red bar), and a decrease in the axial spatial resolution (r_1 versus r_0). Refraction and reflection at phase boundaries in 3D structured samples additionally contribute to optical artifacts (R), and scattering and absorption generally reduce signal intensity with increasing focus depth. (c) In serial section Raman tomography, semithin or ultrathin sections are imaged after producing sequential sections by ultramicrotomy. (d) Tomograms are obtained by stacking images of sections, which avoids artifacts induced by refraction and increases depth resolution. In serial section Raman tomography, axial resolution is defined by section thickness (t), which allows to circumvent the classical resolution limit of confocal microscopy [Colour figure can be viewed at wileyonlinelibrary.com]

chemical structure of a sample can be determined by changes in the Raman spectrum.[4] Consequently, Raman imaging is a well-suited characterization tool for polymers, despite the inferior spatial resolution of confocal light microscopy compared with electron microscopy.[5] Besides obtaining single spectra or 2D images from sample surfaces, confocal microscopy also provides the option to perform optical sectioning as depicted in Figure 1a: imaging at different planes beneath the surface of a specimen.[6]

Confocal microscopy requires highly transparent samples with minimal absorption and scattering of the laser light for obtaining signals from deep within a sample The technique is commonly used in life sciences for the analysis of cells and biological tissues that are stained with fluorescent dyes, where it typically reaches penetration depths of about 100 μm.[6] Compared with fluorescence, the Raman scattering cross section is much smaller and therefore already in ideal cases requires high-intensity laser sources to obtain sufficient signal intensities.[7,8] At the same time, laser power needs to be strictly limited in order to avoid local thermal degradation of the sample during imaging.

Inherent difficulties are linked to confocal imaging below the sample surface. Microscope objectives are optimized for focusing light in a medium of a specific refractive index, and spherical aberration occurs as soon as a phase boundary to a material with a different refractive

index occurs along the beam path.[9] Figure 1b highlights the most serious artifacts from refraction in a simplified manner: spherical aberration leads to a lower signal intensity with increasing focus depth, caused by an axial broadening of the focus spot. As a result of this broadening, the axial resolution of the microscope is reduced (r_1 and r_0 in Figure 1b), and a shift between apparent and actual axial focus position of the microscope is induced (Δz in Figure 1b). Data quality additionally deteriorates in 3D structured samples because of refraction and reflection at internal phase boundaries (R in Figure 1b)[10] and in general light absorption and scattering reduce the achievable imaging depth.

Confocal microscopes for application in life sciences are equipped with immersion objectives that are designed to match the refractive index of the investigated biological tissues, which alleviates the abovementioned issues. In materials science, a broad variety of samples is of interest for chemical imaging, often without established protocols for preparing them for microscopy. Thus, confocal Raman microscopes for broad application ranges are operated with metallurgical objectives. This type of objective works without immersion liquid and without cover slip on the sample surface, which allows imaging on most samples straightforward and with minimal preparation. On the other hand, gross artifacts occur due to refraction when imaging below the sample surface is conducted.[11]

It has been shown that the use of immersion objectives also in materials science is a simple way to mitigate refraction-induced artifacts,[9] but any deviation in the refractive indices of immersion liquid and different sample components deteriorate the resolution of confocal microscopy and would require sophisticated adaptive optics for compensation.[12] There are several restraints for the use of immersion objectives in Raman imaging. Limiting factors are, for example, Raman-active immersion liquids that interfere with signals obtained from the sample or undesirable interactions between liquid and sample. Even if cover glasses between liquid and sample are used to prevent direct contact between both, it is mandatory for the application of immersion objectives to avoid air gaps between sample and cover slip, which is not possible with every sample material.

With serial section Raman tomography, we combine for the first time serial sectioning of a sample with subsequent Raman imaging to overcome the limitations of confocal tomography (Figure 1c). Using the ATUMtome (automated tape collecting ultramicrotome), sequential ultrathin (<200 nm) or semithin (200 nm to 2 μm) sections are cut from a sample with a diamond knife and collected on tape.[13] In a second step, these sections are imaged by confocal Raman microscopy, and a 3D reconstruction of the original sample is generated by stacking the single images (Figure 1d). This approach is inherently destructive, but on the other hand, we aim to prevent artifacts from refraction by avoiding imaging below the sample surface. Therefore, 3D imaging of optically challenging samples like complex polymer blends becomes feasible. Additionally, the depth resolution can be increased compared with confocal microscopy by reducing section thickness (Figure 1d).

Sectioning of samples and subsequent imaging of sections or remaining sample surfaces is a common microscopic technique that can be combined with various imaging modalities such as bright-field,[14] multiphoton,[15] or electron microscopy.[16] Automated sectioning is particularly important for reliable and large-scale tomography,[17] and the ATUMtome allows to collect large numbers of sections simply and reliably on various substrates. It was originally developed for life science applications and has already shown its potential by collecting more than 1,000 ultrathin sections of brain tissue for electron microscopy.[18] Serial section Raman tomography is similar to array tomography, which was developed for correlative volume imaging in life sciences,[19] but this method so far was never combined with confocal Raman microscopy.

In this study, we provide an in-depth comparison of serial section Raman tomography to standard confocal Raman microscopy used for 3D imaging. In both methods, image contrast is solely based on intrinsic differences in the Raman spectra of the investigated sample. With a 3D-structured sample made from polylactic acid (PLA) and polystyrene (PS), we show that our new approach can not only exceed standard confocal Raman microscopy in the achievable imaging volume, but also in terms of axial spatial resolution.

2 | EXPERIMENTAL

2.1 | Sample preparation and serial sectioning

A polymer blend of PS and PLA was prepared by dissolving both polymers (1:1 weight ratio) in dichloromethane. The dispersion was precipitated in ethanol, and the polymer blend was allowed to dry at room temperature. Subsequently, the PS/PLA blend was hot-pressed at 110°C. In order to generate a solid block for ultramicrotomy, hot-pressing was performed several times and with stacking of multiple layers of the blend.

Serial sectioning was performed using an ATUMtome (RMC Boeckeler) equipped with a Diatome Histo (500 nm section thickness) or a Diatome ultra 45°

(100 nm section thickness) diamond knife. Sectioning was performed at room temperature and deionized water was used as floating liquid in the boat. Prior to sectioning, the specimen was trimmed to a rectangular block face using a Diatome trim 90, which ensured constant section size for serial sectioning. Section collection with the ATUMtome was performed on an aluminum-coated polyethylene terephthalate tape of 50 μm thickness and 8 mm width (Goodfellow ES301955).

2.2 | Raman imaging

Imaging of sections was conducted with a confocal Raman microscope (WITec alpha 300). The system was equipped with a 532-nm laser operated at 8 mW. The microscope was coupled to a WITec UHTS 300 VIS–NIR spectrometer connected to a thermoelectrically cooled charge-coupled device (CCD) camera. The spectrometer was equipped with a 300-gr/mm optical grating, leading to a spectral resolution of approximately 8.2 cm^{-1}. A dry objective (Zeiss Epiplan-Neofluar 100×/0.9) was used for imaging. Pixel sizes for Raman imaging were set to meet the nominal section thickness (500 × 500 nm^2 for 500 nm sections; 100 × 100 nm^2 for 100 nm sections), and the integration time was reduced to the device's lower limit of approximately 34 ms/pixel. For the semithin 500 nm sections, a cubic volume of 40 × 40 × 40 μm^3 was imaged (large volume tomogram). An edge of the sections was used to identify the region of interest on each section. Image acquisition took approximately 5.5 min per section. For the ultrathin 100-nm sections, a volume of 10.0 × 10.0 × 2.5 μm^3 was analyzed (high-resolution tomogram). Since exact identification of the region of interest by bright-field microscopy prior to Raman imaging was difficult due to the small field of view, larger images spanning 12.0 × 12.0 μm^2 were taken per section. Imaging time was approximately 10.5 min per section. Confocal Raman tomography of the sample block was performed after serial sectioning with the same equipment and imaging settings, yet with a laser power of 30 mW (100 nm voxel side length) and 50 mW (500 nm voxel side length).

2.3 | Image processing

Background subtraction from spectral data was performed with WITec Project Five+ using the shape-based algorithm of the software at a shape size of 100 and a noise factor of 1. Further processing steps were performed with Matlab (Mathworks). We chose a multivariate phase assignment algorithm that utilizes the complete Raman spectrum of each hyperspectral voxel for generation of false-color tomograms. Compared with evaluating the intensity of single or a few selected vibrational modes, a multivariate method is more robust against single pixel outliers due to cosmic rays and against minor spectral deviations of a component caused by, for example, its molecular orientation relative to the polarization of the excitation laser.[20] Further, the influence of random spectral noise on the result is minimized by this approach. We applied a nonnegative linear least squares algorithm to hyperspectral Raman mappings, as previously described.[21] In brief, the specific spectral contribution of predefined reference spectra to every voxel of a hyperspectral tomogram was determined by this algorithm. Subsequently, data was transformed into stacks of 2D grayscale images in which brightness of a pixel represents the relative contribution of a reference spectrum to this pixel. One 8-bit image stack was created per reference spectrum. High-quality spectra of PS and PLA were recorded separately and were provided to the algorithm as reference spectra (Figure 2).

Image stacks from serial section Raman tomography required image alignment to account for small offsets between the fields of view of images from single sections. Intensity-based image registration was applied on one of the two component stacks, and subsequently the same transformation was applied to the second stack. Rigid image registration was performed, which only allows translation and rotation of single images. In the large volume tomogram (500-nm section thickness), we found that image registration led to a spatial distortion of the image stack as the 3D structure of the PS/PLA blend had a preferential direction that was not perpendicular to the cutting plane. We performed a manual transformation of the image stacks after image registration to realign the stacks toward the cubic volume that they originated from (Figure S1).

In serial section Raman tomography, we identified three main sources of imaging artifacts, which occurred randomly and sparsely distributed on single sections: upon section collection, section folds in the area of interest can occur that lead to parts of a section being out of focus during imaging. Second, contamination with particles on the tape used for section collection or on the surface of sections can occur, which we found causes local thermal degradation of the sample during Raman imaging. Third, and independently from sample and tomographic technique, cosmic rays are a source of artifacts in Raman spectra from spectrometers based on CCD cameras,[22] which can lead to single pixel outliers during phase assignment. We applied median filtering in z-direction with a window size of three voxels to the tomogram from 500-nm sections after phase assignment as a

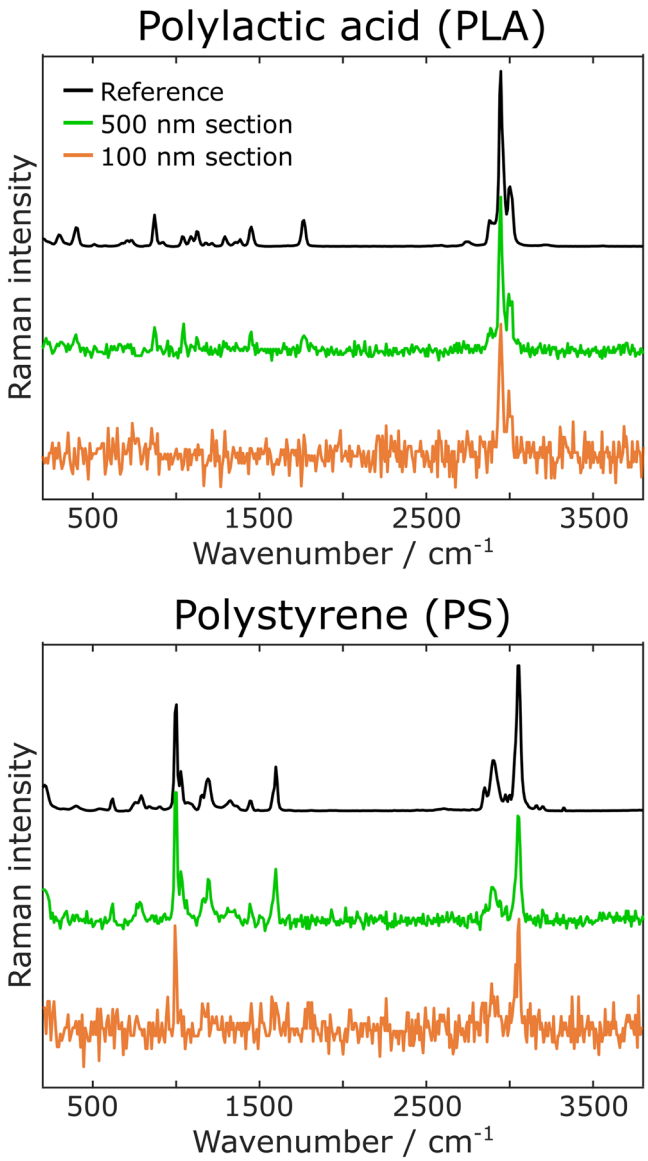

FIGURE 2 Raman spectra of polylactic acid (PLA) and polystyrene (PS). Provided are high-quality reference spectra (upper lines, black) as well as spectra of single pixels from Raman imaging of semithin sections (center lines, green) and from imaging of ultrathin sections (lower lines, orange). Spectra are area-normalized to the displayed spectral range (200 to 3,800 cm^{-1}). Signal-to-noise ratio is reduced in spectra from sections due to low integration time and additionally because of the reduced sampling volume (especially for ultrathin sections) [Colour figure can be viewed at wileyonlinelibrary.com]

simple and efficient tool to minimize the influence of these artifacts (Figure S2). The tomogram from 100-nm sections was processed by a 3D median filter with a window size of three voxels along all three axes to compensate for the aforementioned artifacts and to additionally account for the low signal-to-noise ratio of Raman spectra from ultrathin sections.

Section compression from ultramicrotomy was determined by comparing the size of the sample block face after serial sectioning with the sizes of sections on tape (Figure S3). We found that semithin sectioning led to 29% compression along the cutting direction and ultrathin sectioning to 30% compression. No change in section width (orthogonal to the cutting direction) was observed. Thus, we scaled up the datasets along the affected axis with bicubic interpolation to restore the original block face size (×1.40 for the large volume tomogram and ×1.43 for the high-resolution tomogram). Final datasets spanned 112 × 80 × 80 voxels (56 × 40 × 40 μm^3, large volume tomogram) and 143 × 100 × 25 voxels (14.3 × 10.0 × 2.5 μm^3, high-resolution tomogram).

Data from confocal Raman tomography was directly transformed into stacks of 8-bit grayscale images after phase assignment. The tomograms were scaled up axially with bicubic filtering by a factor of 1.53 in order to at least partially compensate for axial compression because of spherical aberration. This factor was chosen according to the mean difference in refractive indices of PLA ($n = 1.46$)[23] and PS ($n = 1.60$)[24] compared with air since a metallurgical objective was used for imaging. Note that this rough compensation was applied under the assumption of a local 1:1 volume ratio of both polymers and that it does not take into account that the microscope's focus spot is axially enlarged by spherical aberration. Therefore, it presumably still underestimates axial compression.[25]

Finally, false-color Raman images were obtained by assigning different colors to the individual image stacks of PLA and PS (red and blue) and by merging the data to RGB-images in ImageJ. The workflow for all data processing steps is depicted in Figure S4. High-resolution figures for the manuscript were created by upscaling single through-plane images from tomograms 10× with nearest neighbor interpolation to increase image resolution while maintaining original voxel sizes. 3D images and movies of tomograms were created with CTVox (Bruker microCT). Video S1 (confocal Raman tomography at 500 nm voxel side length) and Video S2 (serial section Raman tomography at 500 nm voxel side length) cover an imaging depth of 40 μm. Video S3 (confocal Raman tomography at 100 nm voxel side length) and Video S4 (serial section Raman tomography at 100 nm voxel side length) cover an imaging depth of 2.5 μm.

2.4 | Quantification of tomographic data

Volume proportions in tomograms from serial section Raman tomography were determined by simple

counting of voxels after grayscale thresholding. Image processing resulted in 8-bit image stacks for PLA and PS, each covering the intensity range from 0 to 255. Intensity values greater than 127 were positively segmented, and the resulting binary data was used for quantitative evaluation. No correction for double-positive segmented voxels was performed as they were negligible in our data (23 of 716,800 voxels in the large volume tomogram, and 2 of 357,500 voxels in the high-resolution tomogram).

Domain size distribution was determined by calculating local thicknesses within segmented volumes using a custom-built Matlab code. See Figure S5 for an illustration of the calculation. For histogram representation, the data was normalized to the total voxel count per chemical phase and binned to 250-nm intervals (100-nm sections) or 1-μm intervals (500-nm sections). Anisotropy within the large volume tomogram was evaluated by determining the mean chord length along 25,000 random directions with a custom-built Matlab code. Refer to Figure S6 for more details regarding this analysis. For graphical representation, these values were plotted as a mesh grid on a sphere with interpolated triangle surfaces, where each point corresponds to the direction of its linear connection toward the center of the sphere. Brightness corresponds to the mean chord length in the direction indicated by the position on the sphere. Brightness was scaled between black (4.3 μm) and white (10.3 μm, the highest mean chord length found in the data), and no values smaller than the mean value of the chord length distribution (4.3 μm) are shown on the sphere. Raw and processed imaging data as well as custom Matlab codes for Raman data processing and quantification of tomographic data are available from the corresponding author on request.

3 | RESULTS AND DISCUSSION

3.1 | Large volume tomograms

A 3D-structured polymer blend made from PLA and PS was investigated by confocal Raman tomography, which employs optical sectioning using a confocal microscope, and by Raman imaging of a series of sequential sections. Serial section Raman tomography was performed at a section thickness of 500 nm and at a pixel size of 500 × 500 nm^2 on 80 sequential sections, and we compared the obtained tomogram with optical sectioning at equal voxel size (Videos S1 and S2). Note that both datasets were gathered on the same sample, yet at different locations since the topmost layers of a sample are lost when performing (serial) sectioning with ultramicrotomy.

Data obtained from confocal depth profiling suffered from a severe loss in quality with increasing focus depth, which can be seen in the through-plane Raman image in Figure 3a by blurring between the two phases. A rapid loss in signal intensity occurred with increasing focus depth, which resulted in spectra with a poor signal-to-noise ratio (Figure S7). Between 10 and 15 μm below the sample surface, spectral data was of insufficient quality for a reliable phase assignment, whereas imaging of sections cannot suffer from a loss in signal quality with increasing imaging volume. Consequently, serial section Raman tomography allowed us to image a larger volume at a high and constant quality (Figure 3b), enabling a complete 3D reconstruction of the original sample volume (Figure 3c).

The specific Raman activity of different sample components is of importance whenever mixed spectra occur, as the employed phase assignment algorithm is based on evaluating relative spectral intensities. In our sample, we found that the summarized spectral intensity of PS is about 1.7 times stronger than that of PLA by comparing the raw intensity from single pixels of 500 nm sections (Figure S8). Pronounced "contamination" of confocal tomographic data with PS signal has to be expected at small PLA-features of the sample due to impaired resolution. Out-of-focus contribution additionally influences the spectra of voxels in confocal Raman tomography: the objective does not only illuminate the focus point, and Raman scattering can occur at any illuminated spot, although most of the detected photons are scattered within the focal volume.[9] Refraction reduces the laser intensity at the ideal focus point, despite the total laser power used to irradiate the sample being constant. Thus, out-of-focus contribution increasingly influences spectra at larger focus depths below the sample surface. Small feature sizes, impaired axial resolution, and out-of-focus contribution explain why the PLA signal becomes blurred and weak directly below the surface and why at larger focus depths only PS signal is observed in confocal Raman tomography (Figure 3a). We exclude that the algorithm we employed for phase assignment led to an intrinsically biased result that favored PS over PLA, since neither blurring of features nor weak PLA representation were found in serial section Raman tomography (Figure 3b).

3.2 | High-resolution tomograms

Next, we performed serial sectioning of the PS/PLA blend at a section thickness of 100 nm. Theoretically,

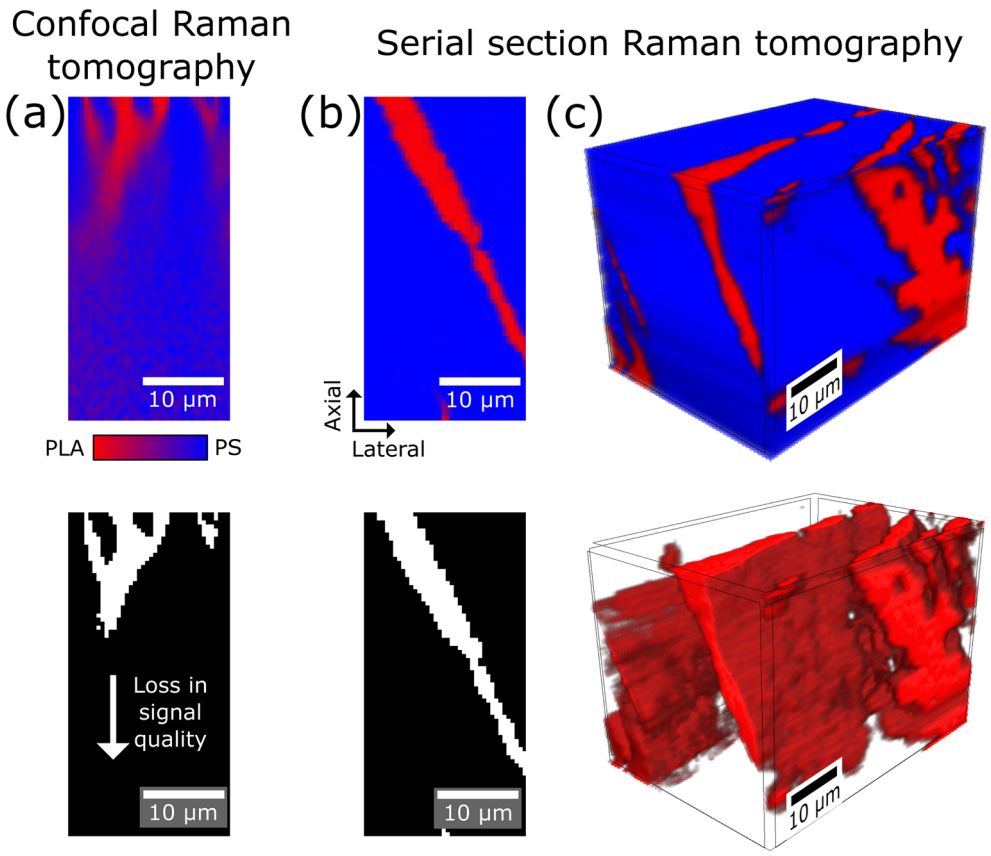

FIGURE 3 Comparison of large volume tomograms (500 nm voxel side length) from confocal and serial section Raman tomography. (a and b) Through-plane images from volumes imaged by (a) confocal Raman and (b) serial section Raman tomography. Note that the tomograms were not acquired at identical positions of the sample. Data from confocal Raman tomography is compensated for spherical aberration by axial upscaling (×1.53). The upper images show spectral contributions of polylactic acid (PLA) (red) and polystyrene (PS) (blue), whereas the lower images are segmented for PLA by a simple threshold (≥0.5). (c) The complete volume imaged by serial section Raman tomography after correction for section compression ($56 \times 40 \times 40\ \mu m^3$), with signals of PLA and PS in the upper image and only the spectral contribution of PLA in the lower image. For a clearer representation, for both phases voxels with an intensity less than 0.2 are not displayed in (c) [Colour figure can be viewed at wileyonlinelibrary.com]

confocal microscopy can reach a depth resolution of about 1 μm (Figure S9), but the axial resolution is worse in real applications and typically in the range of several microns: as soon as refraction at phase boundaries between air and sample (metallurgical objectives), between immersion liquid and sample (immersion objectives), and between different phases within a sample occurs, depth resolution is impaired.[11] Axial resolution is defined by section thickness when imaging of sequential sections is performed (Figure 1d), and it has already been shown that the classical resolution limit of confocal microscopy can be circumvented with this approach.[19] Figure 4 compares confocal Raman tomography at 100 nm voxel side length with serial section Raman tomography of 100-nm sections imaged at a pixel size of $100 \times 100\ nm^2$ (see also Videos S3 and S4). Inferior data quality from optical sectioning can be observed by blurring of features in Figure 4a: influence of structures from below and above the focus points led to mixed spectra to which both PLA and PS contributed. This phenomenon can be explained by the fact that features within the sample are as small as 1 μm and less (Figure 4b). Therefore, mixed spectra of both polymers generally have to be expected because of the diffraction limited resolution of confocal microscopy. On the other hand, serial section Raman tomography remained unaffected by this effect and therefore allowed us to perform tomography beyond the achievable spatial resolution of confocal microscopy and despite the inherently weak Raman effect (Figure 4c).

Collection and imaging of sections was performed on an aluminum-coated tape. The metal coating prevents evoking Raman signals from the polymer tape, which would otherwise lead to spectral contamination by the substrate if a polymer or glass was used. Thus, pure spectra from sections were recorded at an effective depth

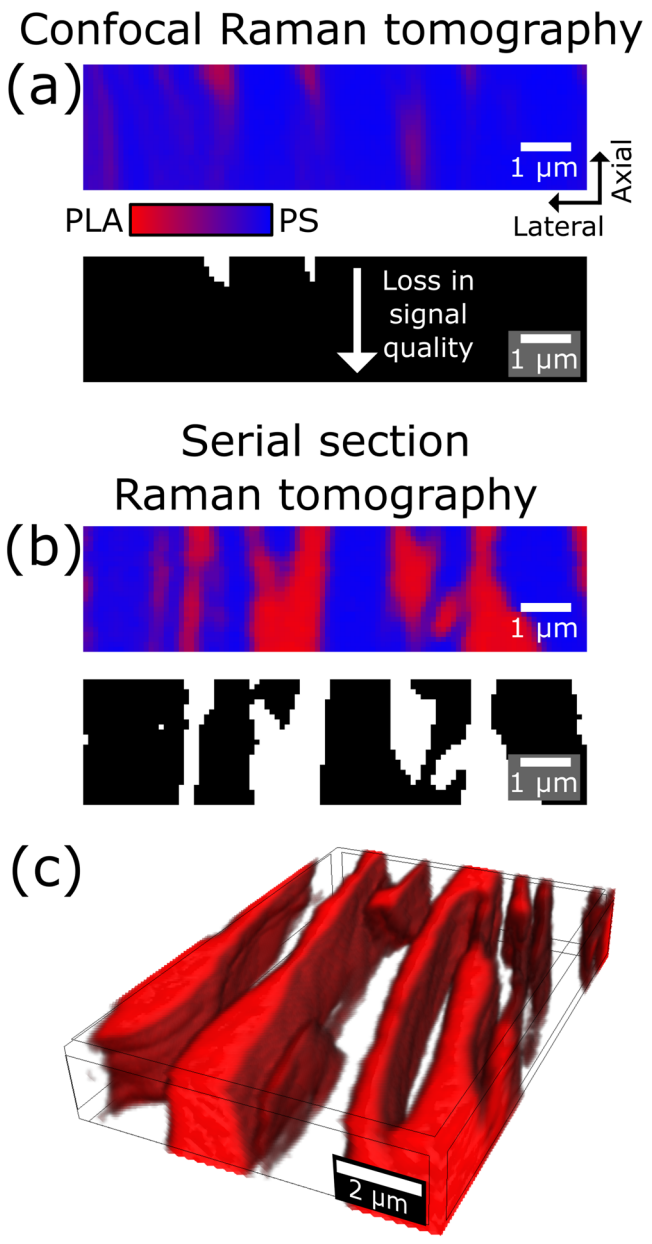

FIGURE 4 Comparison of high-resolution tomograms (100 nm voxel side length) from confocal and serial section Raman tomography. (a and b) Through-plane images from volumes imaged by (a) confocal Raman tomography and (b) serial section Raman tomography. Note that tomograms were not acquired on identical positions of the sample. Data from confocal Raman tomography is compensated for spherical aberration by axial upscaling (×1.53). The upper images in each panel show spectral contributions of polylactic acid (PLA) (red) and polystyrene (PS) (blue), whereas the lower images are segmented for PLA by a simple threshold (≥0.5). (c) Signal of PLA in the complete volume imaged by serial section Raman tomography after correction for section compression ($14.3 \times 10.0 \times 2.5\ \mu m^3$). For a clearer representation, voxels with an intensity less than 0.2 are not displayed in (c) [Colour figure can be viewed at wileyonlinelibrary.com]

resolution equal to section thickness. It is particularly important to obtain pure sample spectra for successful phase assignment in hyperspectral images from ultrathin sections: in order to minimize time required for imaging, the integration time per pixel was set to the device's technical limit of about 34 ms. While the signal intensity of semithin 500-nm sections from the large volume tomogram at this low integration time was still at around 1,450 counts per voxel (median of 1,443 counts in the spectral interval from 200 to 3,800 cm^{-1}, after background removal), the small sampling volume in imaging of ultrathin sections became apparent by noisy spectra with less than 500 counts (median of 458 counts) of the high-resolution tomogram (Figure 2). As a comparison, the signal intensity of the reference spectra shown in Figure 2 was more than 600,000 counts. Nevertheless, chemical phase assignment was robust as no Raman signals other than pure spectra from the ultrathin sections were evoked.

Imaging time is a critical factor in confocal Raman imaging. In comparison with other imaging techniques, relatively long integration times per pixel are required for collecting hyperspectral Raman images. For example, taking a single 2D image of the high-resolution tomogram (120 × 120 pixels) required approximately 10.5 min. There have been attempts to increase speed of Raman imaging by, for example, combining a light sheet microscope with Raman spectroscopy,[26] but in the end, laser power remains as a limiting factor that can cause sample drift and thermal degradation during imaging. In our work, integration time per pixel was set as low as possible to evaluate the minimum signal quality required for successful imaging. At least for imaging of semithin sections of the PS/PLA blend we see potential to further reduce the integration time per pixel: even the lower signal to noise ratio from ultrathin sections was still sufficient for a robust phase assignment. The speed of confocal Raman tomography is nevertheless out of reach with serial section Raman tomography, due to its more time-consuming sample preparation.

We find that the serial section approach is advantageous in avoiding sample drift. In confocal tomography, constant input of heat by laser irradiation for several hours during Raman imaging possibly leads to thermal expansion and therefore a drift of the sample, which can severely impair data quality of high-resolution tomograms. The risk of sample drift is minimal in serial section Raman tomography, as no bulk sample is imaged, only a few minutes are spent on imaging a single section, and a relatively low laser intensity is employed. Serial section Raman tomography may lead to a similar artifact, a spatial distortion of the image stack caused by image

registration of the single images. In this case, the original volume shape can be simply restored by transforming the image stack toward the original rectangular sample block.

3.3 | Feasibility of quantification of volume properties

High-quality tomograms allow to quantify structural properties and structure-derived parameters from a specimen. Data from confocal tomography was scaled up axially as a rough compensation for artifacts induced by refraction. However, this correction cannot take the full complexity of optical artifacts from the inhomogeneous sample into account.[27] In addition to the inevitably remaining spatial inaccuracy, phase assignment was not reliable due to insufficient resolution, out-of-focus contribution, and poor signal-to-noise ratio: the data from confocal Raman tomography was not adequate for an analysis of the sample's 3D structure. While serial section Raman tomography is unaffected from these optical issues, physical sectioning leads to section compression as an artifact. We compensated the data for section compression by uniaxial upscaling of the single images.

Tomograms from serial section Raman tomography showed high discriminability between the two polymers in the PS/PLA blend. Using a straightforward threshold segmentation, we found that 13.8% of the volume imaged from 500-nm sections consisted of PLA, and 84.3% of the volume was PS. 1.9% of the voxels neither consisted of greater than or equal to 50% PLA nor greater than or equal to 50% PS. Small offsets in the fields of view between single sections led to a small volume fraction of 1.9% with missing information, as image registration was performed prior to segmentation. The volume proportions of the polymers remained almost constant (less than 3% deviation) when we accounted for the different spectral intensities of PS and PLA by using a weighted threshold segmentation (≥37% for PLA and ≥63% for PS). We conclude that the simple threshold segmentation is robust on tomograms from this sample system. Weighted threshold segmentation or phase assignment with intensity-weighted reference spectra are possible means to compensate for differences in the Raman scattering cross sections between different phases in multicomponent samples. In the tomogram obtained from 100-nm sections, a larger field of view was imaged initially, and only a subset of the original field of view was processed after image registration to minimize missing information due to an offset between single sections. In this volume, we found that 35.5% of all voxels consisted of PLA, while 64.5% contained PS, and less than 0.1% were ambiguous.

As the different volume proportions of the two tomograms reveal, the PS/PLA blend sample is a microscopically heterogeneous sample. The sampled volumes are not representative for the whole sample. Nevertheless, we performed basic quantitative analyses to exemplarily show some parameters that can be obtained from tomograms. Figure 5 displays the domain sizes of the two components within the tomograms: local thicknesses of both PLA and PS were computed and are provided as histograms. Domain size in polymer blends is an important factor that determines, for example, mechanical

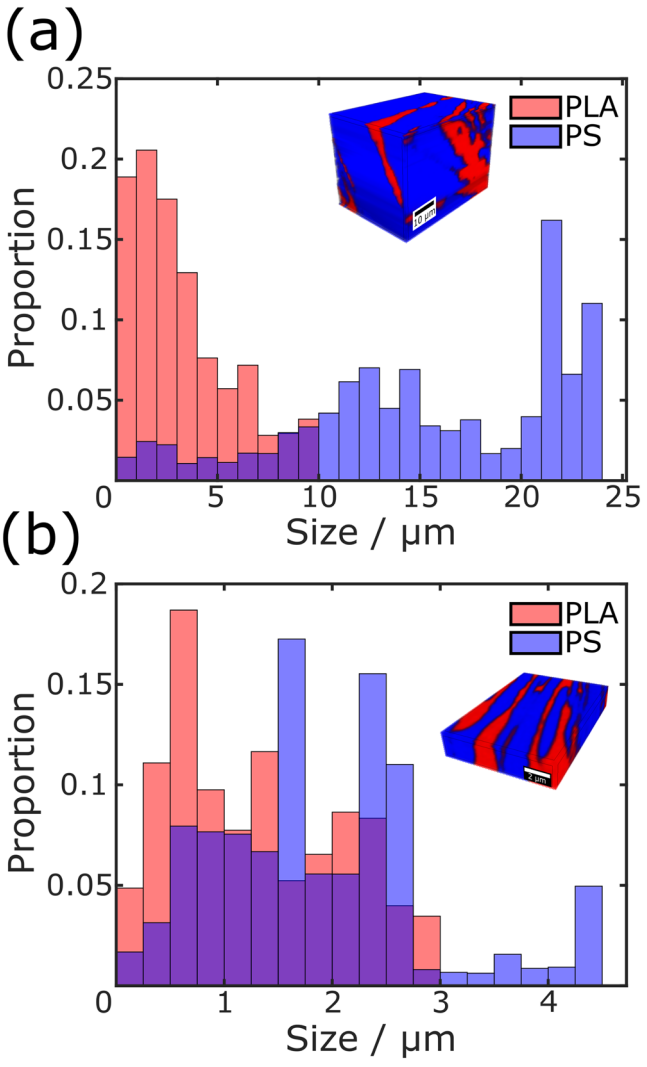

FIGURE 5 Domain size distribution in (a) large volume and (b) high-resolution tomograms from serial section Raman tomography. Local thicknesses of polylactic acid (PLA) and polystyrene (PS) within the tomograms were computed and are provided as histogram plots. Data is given relative to the total number of voxels of each component [Colour figure can be viewed at wileyonlinelibrary.com]

parameters of the bulk sample.[28] Formation of larger or smaller domains of immiscible polymer blends can be controlled, for example, by compatibilizers,[29] and a reliable 3D characterization can assist in elucidating relations between variables in processing and properties of the end product.

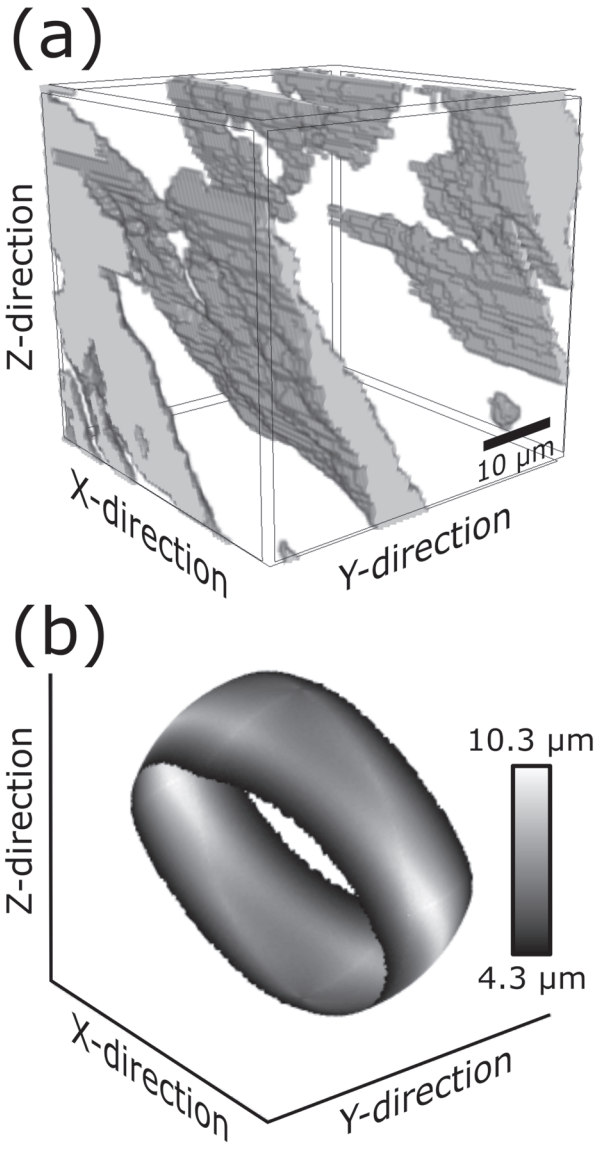

FIGURE 6 Determination of anisotropy in the large volume tomogram from serial section Raman tomography. (a) Cubic part of the tomogram (80 × 80 × 80 voxels) with segmentation of polylactic acid (PLA). (b) Chord length distribution of the structure shown in (a). Mean chord length along different directions was determined and results are displayed as brightness on the surface of a sphere. The linear connection between surface and center of the sphere represents the direction, and brightness indicates the corresponding mean chord length. Since only values higher than the mean chord length of the structure (4.3 μm) are shown, the sphere is not completely visible: anisotropy of PLA in the volume in (a) occurs as a preferential direction along the plane that is given by the ring in (b)

Further, serial section Raman tomography revealed that the distribution of PLA and PS is anisotropic (Figure 3c). We computed the chord length distribution of PLA within the large volume tomogram, which confirmed that the PLA domain is mainly oriented along a preferential plane (Figure 6). This finding can be easily traced back to sample preparation, as hot-pressing of the polymer blend was part of the manufacturing process. Anisotropy is required in functional materials that need to exhibit different properties in different directions, for example, to act as a barrier along a specific plane.[28] In other applications, anisotropy may be an undesired result from production that needs to be minimized in order to obtain a macroscopically homogeneous material. In both cases, evaluation of anisotropy by tomography is a valuable tool for sample characterization.

4 | CONCLUSION

In this study, we showed for the first time that serial sectioning of a sample can be successfully combined with Raman imaging to obtain reliable tomograms of a specimen. Using an ultramicrotome with automated section collection (ATUMtome), we created and imaged series of semithin and ultrathin sections of a PS/PLA blend, followed by 3D reconstruction of its inner structure. Further, we exemplarily quantified structural parameters in the investigated volumes.

In comparison with optical sectioning with confocal microscopy, the serial section approach requires sample destruction and is more labor intensive due to additional time spent on physical sectioning, sequential imaging, and data processing. On the other hand, severe artifacts from refraction that prevent reliable confocal 3D imaging are effectively eliminated. Consequently, serial section Raman tomography is suitable for an accurate tomography of various samples, irrespectively of changes in the refractive index within their inner structure. In addition, samples of low light transmittance can be imaged after serial sectioning, which would otherwise result in limited penetration depth in confocal microscopy.

While superior 3D data quality can be obtained from serial section Raman tomography, the approach is limited to samples that allow processing by ultramicrotomy. The use of (ultra)microtomes is widely established in life sciences but may fail on samples in materials science due to, for example, a low glass transition temperature of polymers or components with weak interfaces that separate upon sectioning. Cryo-ultramicrotomy is a workaround to obtain sections from demanding samples for electron microscopy,[3] but, to our knowledge, is so

far not available in combination with the collection of series of sections on tape. Nevertheless, high-quality sections of many samples can already be obtained at room temperature by using optimized diamond knives.[30] Serial section Raman tomography is a promising imaging method in materials science. Also, we see potential of the technique in life sciences, as, for example, 3D chemical mappings of embedded tissues may be collected: imaging of sections eliminates out-of-focus fluorescent background from the specimen, which may improve signal quality despite low integration times per pixel. However, imaging speed and data processing of hyperspectral images need to be reevaluated in the analysis of complex biological tissues.

Resolution and field of view of serial section Raman tomography can be adjusted according to the requirements of the sample system. Similar to array tomography, where section thickness defines the axial resolution,[19] we showed that it is possible to circumvent the classical resolution limit of confocal Raman microscopy by imaging of ultrathin sections: A depth resolution of 100 nm was achieved with serial section Raman tomography. In the future, imaging of ultrathin sections may be complemented with tip-enhanced Raman spectroscopy as a super-resolution imaging method,[31] which may allow 3D Raman imaging with isotropic voxel sizes in the two-digit nanometer range. In addition, correlative imaging that combines, for example, electron and Raman microscopy may be performed on serial sections, similar to array tomography in life sciences,[19] to gain a more thorough understanding of the investigated sample systems.

ACKNOWLEDGEMENTS

The authors thank Dr Ralf Thomann for providing sample material and Britta Mayerhöfer for assistance with manufacturing of the polymer blend. The authors gratefully acknowledge funding by the German Federal Ministry of Education and Research (BMBF): grant number 03SF0536F (project Power-MEE).

CONFLICT OF INTERESTS

The authors declare no conflict of interest.

ORCID

Thomas Böhm https://orcid.org/0000-0003-2036-2159
Simon Thiele https://orcid.org/0000-0002-4248-2752

REFERENCES

[1] S. Stewart, R. J. Priore, M. P. Nelson, P. J. Treado, *Annu. Rev. Anal. Chem.* **2012**, *5*, 337.
[2] C. Krafft, M. Schmitt, I. W. Schie, D. Cialla-May, C. Matthäus, T. Bocklitz, J. Popp, *Angew. Chem. Int. Ed.* **2017**, *56*, 4392.
[3] G. H. Michler, *Electron Microscopy of Polymers*, Springer, Berlin, Heidelberg **2008**.
[4] T. Böhm, R. Moroni, M. Breitwieser, S. Thiele, S. Vierrath, *J. Electrochem. Soc.* **2019**, *166*, F3044.
[5] U. Schmidt, J. Müller, J. Koenen, in *Confocal Raman Microscopy*, (Eds: T. Dieing, O. Hollricher, J. Toporski) Vol. 158, Springer. Berlin, Heidelberg **2011** 237.
[6] D. Semwogerere, E. R. Weeks, in *Encyclopedia of Biomaterials and Biomedical Engineering*, (Eds: G. E. Wnek, G. L. Bowlin), Taylor and Francis, London **2005**.
[7] J. B. Pawley, *Handbook of biological confocal microscopy*, Springer, New York **2006**.
[8] E. Smith, G. Dent, *Modern Raman spectroscopy: A practical approach*, Wiley, Chichester **2008**.
[9] N. J. Everall, *Analyst* **2010**, *135*, 2512.
[10] N. J. Everall, *J. Raman Spectrosc.* **2014**, *45*, 133.
[11] N. J. Everall, *Appl. Spectrosc.* **2000**, *54*, 1515.
[12] M. J. Booth, *Light Sci Appl* **2014**, *3*, e165.
[13] P. Webster, D. Bentley, J. Kearney, *Microsc. Anal.* **2015**, *29*(2), 19.
[14] A. Li, H. Gong, B. Zhang, Q. Wang, C. Yan, J. Wu, Q. Liu, S. Zeng, Q. Luo, *Science (New York, N.Y.)* **2010**, *330*, 1404.
[15] L. Abdeladim, K. S. Matho, S. Clavreul, P. Mahou, J.-M. Sintes, X. Solinas, I. Arganda-Carreras, S. G. Turney, J. W. Lichtman, A. Chessel, A.-P. Bemelmans, K. Loulier, W. Supatto, J. Livet, E. Beaurepaire, *Nat. Commun.* **2019**, *10*, 1662.
[16] F. Hegge, R. Moroni, P. Trinke, B. Bensmann, R. Hanke-Rauschenbach, S. Thiele, S. Vierrath, *J. Power Sources* **2018**, *393*, 62.
[17] J. E. Spowart, *Scr. Mater.* **2006**, *55*, 5.
[18] N. Kasthuri, K. J. Hayworth, D. R. Berger, R. L. Schalek, J. A. Conchello, S. Knowles-Barley, D. Lee, A. Vázquez-Reina, V. Kaynig, T. R. Jones, M. Roberts, J. L. Morgan, J. C. Tapia, H. S. Seung, W. G. Roncal, J. T. Vogelstein, R. Burns, D. L. Sussman, C. E. Priebe, H. Pfister, J. W. Lichtman, *Cell* **2015**, *162*, 648.
[19] K. D. Micheva, S. J. Smith, *Neuron* **2007**, *55*, 25.
[20] B. Jasse, R. S. Chao, J. L. Koenig, *J. Polym. Sci. Polym. Phys. Ed.* **1978**, *16*, 2157.
[21] M. S. Mu'min, T. Böhm, R. Moroni, R. Zengerle, S. Thiele, S. Vierrath, M. Breitwieser, *J. Membr. Sci.* **2019**, *585*, 126.
[22] C. A. Murray, S. B. Dierker, *J. Opt. Soc. Am. A* **1986**, *3*, 2151.
[23] M. H. Hutchinson, J. R. Dorgan, D. M. Knauss, S. B. Hait, *J. Polym. Environ.* **2006**, *14*, 119.
[24] N. Sultanova, S. Kasarova, I. Nikolov, *Acta Phys. Pol. A* **2009**, *116*, 585.
[25] S. H. Wiersma, P. Török, T. D. Visser, P. Varga, *J. Opt. Soc. Am. A* **1997**, *14*, 1482.
[26] W. Müller, M. Kielhorn, M. Schmitt, J. Popp, R. Heintzmann, *Optica* **2016**, *3*, 452.
[27] N. J. Everall, *Appl. Spectrosc.* **2000**, *54*, 773.
[28] C. Harrats, S. Thomas, G. Groeninckx (Eds), *Micro- and Nanostructured Multiphase Polymer Blend Systems: Phase Morphology and Interfaces*, Taylor & Francis, Boca Raton **2006**.
[29] R. Muthuraj, M. Misra, A. K. Mohanty, in *Biocomposites: Design and Mechanical Performance*, (Eds: M. Misra, J. K. Pandey, A. K. Mohanty), Elsevier, Amsterdam **2015** 93.
[30] D. Studer, H. Gnaegi, *J. Microsc.* **2000**, *197*, 94.

[31] R. M. Stöckle, Y. D. Suh, V. Deckert, R. Zenobi, *Chem. Phys. Lett.* **2000**, *318*, 131.

SUPPORTING INFORMATION

Additional supporting information may be found online in the Supporting Information section at the end of this article.

How to cite this article: Böhm T, Moroni R, Thiele S. Serial section Raman tomography with 10 times higher depth resolution than confocal Raman microscopy. *J Raman Spectrosc*. 2020;1–12. https://doi.org/10.1002/jrs.5878